Optics & Laser Technology 168 (2024) 109977

Contents lists available at ScienceDirect

Optics and Laser Technology

journal homepage: www.elsevier.com/locate/optlastec

Full length article

3D printed Fabry-Perot acoustic probe with a glass horn tube

Heming Wei [a], Zhangli Wu [a], Yan Wei [a], Chen Wang [b,*], Haiyan Zhang [a], Fufei Pang [a,*], Carlos Marques [c], Christophe Caucheteur [d], Xuehao Hu [d]

[a] Key Laboratory of Specialty Fiber Optics and Optical Access Networks, Joint International Research Laboratory of Specialty Fiber Optics and Advanced Communication, Shanghai University, Shanghai 200444, China
[b] Department of Precision Mechanical Engineering, Shanghai University, Shanghai 200444, China
[c] Department of Physics, University of Aveiro, Aveiro 3810-193, Portugal
[d] Department of Electromagnetism and Telecommunications, University of Mons, Mons 7000, Belgium

ARTICLE INFO

Keywords:
Fabry-Perot
Acoustic wave
Two-photon polymerization
3D printing
Optical fiber sensor

ABSTRACT

Sensing an incoming acoustic signal is typically associated with absorbing the energy, perturbing the measurement and therefore causing a deformation of the sensing elements, which is mainly related to the acoustic wave pressure. Here, we demonstrated a fiber-tip based Fabry-Perot (FP) acoustic probe sensor, which was directly printed on an optical fiber tip by a two-photon 3D printing technique and assembled by a glass horn structure, which can improve the sensitivity. It showed that the sensor has a −3 dB bandwidth of 366.05 kHz at the first resonant frequency of 467.84 kHz. A low noise-limited minimum detectable pressure level of 4.71 mPa/Hz$^{1/2}$@100 kHz is obtained. Due to the acoustic wave focusing property of the horn structure, the detected signal intensity can be amplified by 4 times as the sensor located at the bottom position. It demonstrates that 3D printed micro acoustic devices could be used for weak acoustic wave detection in the applications of partial discharge, photoacoustic imaging and non-destructive detection.

1. Introduction

Acoustic emission (AE) plays a vital role in the fields of aerospace engineering, mechanical engineering, and biomedical engineering, etc., as it can be used for imaging and detecting the fatigued parts at sub-micron scale [1–4]. One of the main components is the acoustic wave sensors. Many optic and piezoelectric sensors have been reported for photoacoustic imaging [5–7] and structural health monitoring [8,9], among other applications. Compared with piezoelectric transducers [10], the optical AE sensors exhibit many merits, such as compact size, immunity to electromagnetic interference, high sensitivity and wide bandwidth [11,12]. Until now, various optical AE sensors have been studied, such as interferometers [13–15], micro-rings resonators [16–18], grating-based sensors [19–23]. Among these sensors, Fabry-Perot (FP) interferometers have attracted great attention for their compact structures. However, the sensitivity of FP-based AE devices is still a critical issue.

Different works have been done to improve the pressure sensitivity. For diaphragm-based FP sensors, sensitive vibrating diaphragms made of metal [24], silicon [25], graphene [26,27], polymer [28,29] and chitosan [30] have been used to enhance the pressure sensitivity of the FP acoustic sensor due to its outstanding mechanical properties like low Young's modulus. Noted that the sensitivity increases as the diaphragm's thickness decreases. Therefore, various fabrication methodologies, such as splicing and chemical vapor deposition, are used for fabricating thin diaphragms with thickness at nanoscale. However, tremendous difficulties appear with the fabrication of a diaphragm with a thickness below sub-micrometers [31]. Additionally, novel proper design can achieve a relative high sensitivity. Zhang *et al.* designed spiral microbeam-based FP devices by a 3D μ-printing technique, which can reach a high sensitivity of 118.3 mV/Pa and a low noise equivalent acoustic signal level of 0.328 μPa/Hz$^{1/2}$ at audio frequency [32]. A plano-concave microcavity can be designed and fabricated for flexible FP sensors, which has a bandwidth of nearly 20 MHz and sensitivity is approximately 2.82 mV/kPa [33]. Guggenheim et al. fabricated a plano-concave polymer FP cavity for ultrasound detection, which showed a broadband acoustic response of 40 MHz and a noise-equivalent pressure of 1.6 mPa/Hz$^{1/2}$[34]. Noted that the fabricated device should have a high optical or acoustic quality factor to achieve a high sensitivity, however, the fabrication could be relatively complicated. Recently, the

* Corresponding authors.
E-mail addresses: chenwang@shu.edu.cn (C. Wang), ffpang@shu.edu.cn (F. Pang).

https://doi.org/10.1016/j.optlastec.2023.109977
Received 17 May 2023; Received in revised form 28 July 2023; Accepted 21 August 2023
Available online 25 August 2023

direct laser writing technique through two-photon polymerization is commonly used for fabrication of micro-optical devices for sensing applications [17,22,35,36]. Although this technique has a relatively high resolution, the optical/acoustic quality factor of fabricated devices is relatively low. In comparison, sound focusing structures, such as concave acoustic focusing lens [37], flat Fresnel zone plates (FZP) lens [38] and acoustic *meta*-material [39], are one of the most efficient ways to achieve high sensitivity. Combined with miniature optical microphones, the horn structure can be a simple and effective way to further improve the encapsulated fiber tip-based FP AE sensors.

In this work, we proposed a glass horn structure encapsulated FP AE sensor, in which the FP device was directly fabricated on a fiber tip by the two-photon 3D printing technique. The sensor consists of a diaphragm with a thickness of 5 μm supported by four circular pillars. To investigate the sensing performance, the mode coupling behavior between the diaphragms and supporting pillars is investigated. To further improve sensitivity, a glass horn tube (GHT) is used for assembling the device as a probe sensor, which plays a role of sound focusing waveguide. The test results show that the intensity of detected signal at 500 kHz can be greatly improved by 4 times compared the sensor without GHT. Besides, the sensor has a first-order resonant frequency of 476.84 kHz and −3 dB bandwidth of 366.05 kHz. It demonstrates that the proposed method is promising for fabricating high-sensitive FP AE sensors, which can be used for acoustic wave detection.

2. Design and simulation

2.1. Sensor design

The schematic diagram of the proposed FP AE device is shown in Fig. 1. Fig. 1(a) shows the fiber tip-based FP sensor with a cavity length of 150 μm, a diameter of 100 μm and a 5 μm-thickness diaphragm with variable distances *W* between adjacent pillars. Fig. 1(b) shows the FP acoustic sensor placed at the bottom position inside the GHT, which acts as an ultrasonic horn. It has been precisely designed to intensify the acoustic wave energy and therefore amplify the acoustic pressure. The side view of the device is shown in Fig. 1(c), where r_g and r_a are the radius of the upper and the lower surfaces of the flare, respectively, and *H* is the height of the GHT. Based on the theory of the geometric acoustics, the acoustic wave is reflected and transmitted inside the GHT and get focused at the bottom position [40]. Hence, the sensor can be inserted into GHT for high acoustic pressure sensitivity. The bottom of GHT was set z = 0 mm, and the pressure of the acoustic wave could be influenced if the FP sensor moves along the z-axis, as shown in Fig. 1(c).

Considering the low reflectivity of the fiber end and diaphragm, the FP sensor can be simplified as a two-beam interferometer and the reflection intensity of the sensor can be expressed by [26]:

$$I_R(\lambda) = I_1(\lambda) + I_2(\lambda) + 2\sqrt{I_1(\lambda)I_2(\lambda)} \times cos\left(\frac{4\pi nl}{\lambda}\right) \quad (1)$$

where I_R(Î») is the total intensity of the reflected light, Î» is the wavelength of the laser light, I_1(Î») and I_2(Î») are the reflected intensities around R_1 at the air/diaphragm interface and R_2 at the fiber/air interface. n is the refractive index of the FP cavity, l is the cavity length. When the acoustic is applied on the diaphragm, the diaphragm is vibrated, and this causes a change of cavity length, Δl, thus, the interference intensity change can be illustrated as:

$$\Delta I_R(\lambda) = -\frac{8\pi n}{\lambda}\sqrt{I_1(\lambda)I_2(\lambda)}sin\left(\frac{4\pi nl}{\lambda}\right)\Delta l \quad (2)$$

To ensure high acoustic pressure sensitivity, wide dynamic and linear response range, the wavelength of the input laser light should be fixed at the quadrature point (Q-point) where a maximal linear response to acoustic wave induced phase change can be obtained.

2.2. Simulation

To characterize the dynamic response of the proposed sensor inside GHT in the water environment, the resonant frequency and displacements of the resonant cavity is simulated by a finite elements method (FEM). The density, Young's modulus and Poison ratio of the material (IP-Dip) is 1100 kg/m^3, 3.097 GPa and 0.49, respectively [41]. For the circular-clamped diaphragm-based acoustic sensors, the resonant frequency and acoustic pressure sensitivity are directly related to the diaphragm diameter and thickness. Additionally, the mode coupling could happen as the pillar supports of the device has an impact on the overall resonant frequency of the sensor. Fig. 2(a) shows that the resonant frequency varies with the parameter *W* with a constant incident plane wave pressure of 100 Pa, which shows that the pillars have a slightly coupling influences on the resonant frequency of the diaphragm. The inset of Fig. 2(a) shows the first-order resonant frequencies of the devices with *W* = 0 μm and *W* = 50 μm. The diaphragm displacements at the center point versus applied pressure are simulated as shown in Fig. 2(b), which demonstrates the sensor has a linear response between 10 Pa and 200 Pa. By choosing the suitable *W*, thickness and diameter of the diaphragm, the sensor's resonant frequency and sensitivity can be flexible adjusted.

The acoustic pressure distribution in the GHT is simulated with the incident plane wave of 100 Pa along z-axis. The pressure gain is defined as the ratio of the pressure in different positions along the z-axis to the amplitude of the incident pressure. As observed in Fig. 3(a), the pressure is magnified to 7.42 times in the focal zone located in the bottom of the GHT at a frequency of 500 kHz when r_g, r_a and H are 2 mm, 0.4 mm and 4 mm, respectively. Fig. 3(b) shows pressure gain along the z-axis from 6 mm to −2 mm with different frequencies, which changes along the direction of the acoustic wave propagating and reaches a peak value at a specific position z depending on the frequency. Fig. 3(c) shows the maximum pressure gain and corresponding position along the z-axis at different frequencies. Noted that it can realize a maximum pressure gain within a relatively broadband range when the sensor is set at the bottom position.

To further investigate the frequency response of the FP device with the glass horn structure, Fig. 3(d) shows the displacements of the central

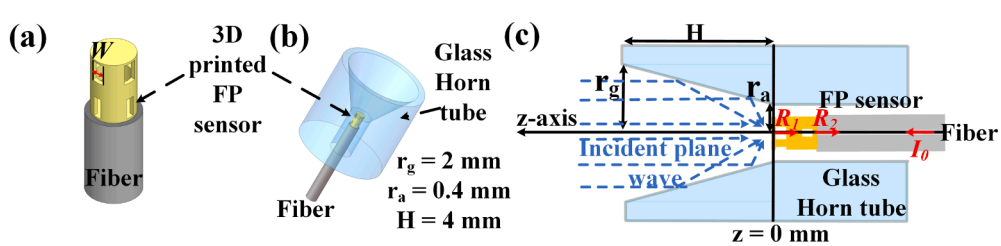

Fig. 1. The Schematic diaphragm of pillars-supported micro-resonator on the fiber tip integrated with a glass horn tube. (a) Schematic diaphragm of the designed acoustic sensor based on pillars-supported micro-resonator on the fiber tip. (b) The Schematic diaphragm of assembled FP sensor inside GHT. (c) The side view of the proposed sensing elements in (b).

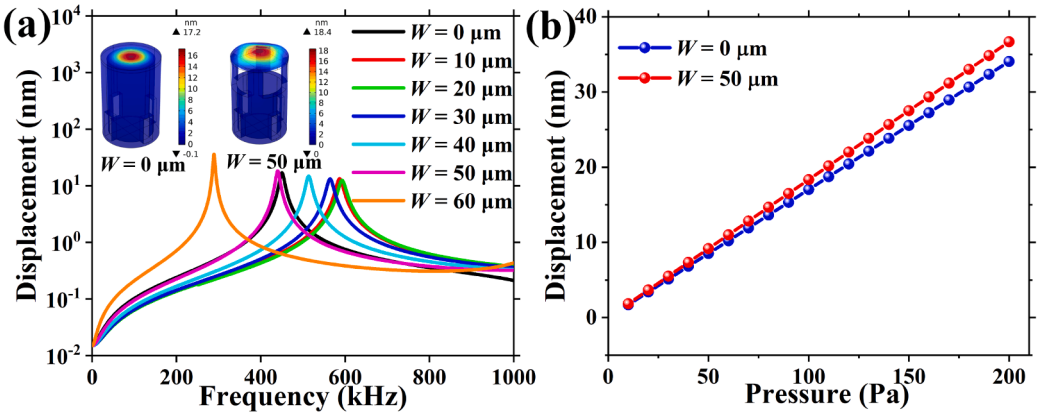

Fig. 2. The simulated resonant frequency and pressure response of the sensor. (a) The first-order resonant frequency response of the diaphragm when a changing W from 0 to 60 μm is used. The insets show the first-order frequencies when $W = 0$ and $W = 50$ μm are selected, separately. (b) The diaphragm displacements of the devices with W = 0 and W = 50 μm versus applied pressures at first-order resonant frequency.

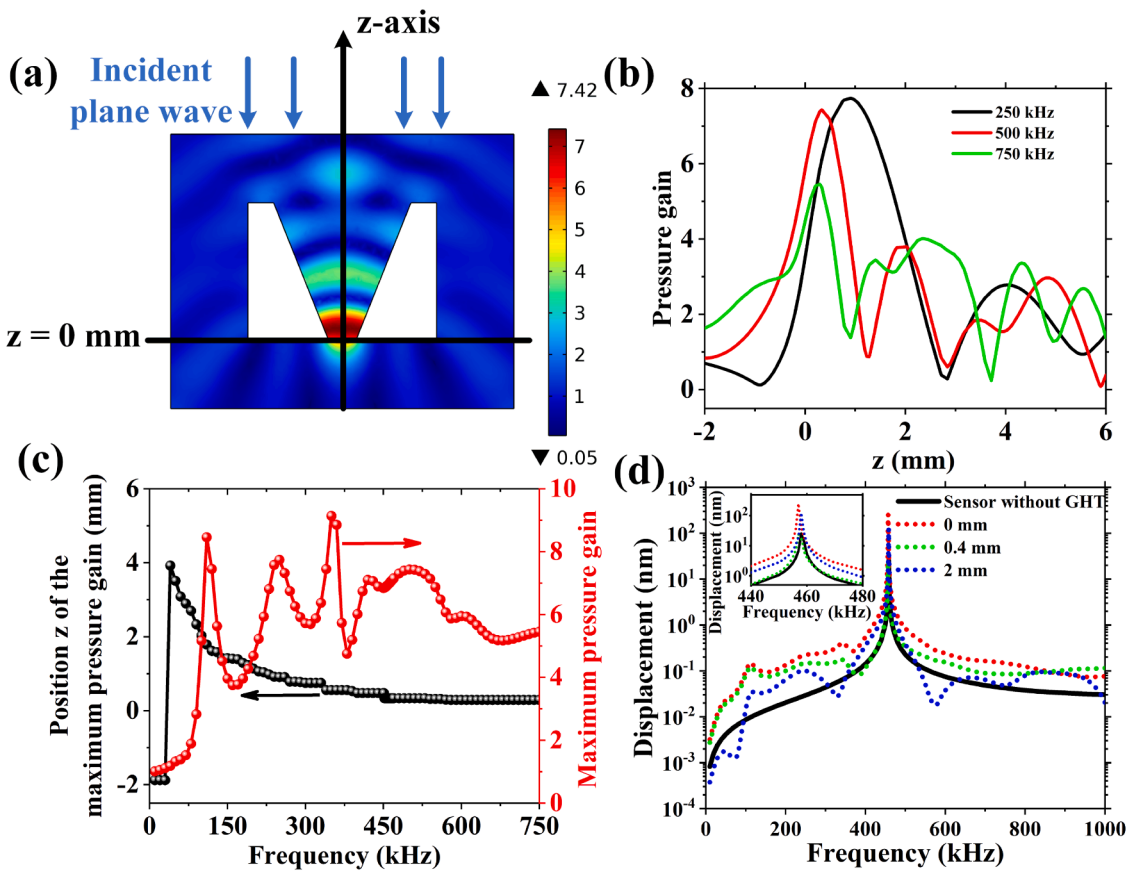

Fig. 3. The simulated focusing process of the GHT. (a) The acoustic wave propagating and focusing process inside of the GHT in water. (b) The pressure gain along the z-axis with different frequencies. (c) The maximum pressure gain and corresponding position along the z-axis with different frequencies. (d) The comparison of displacements of the diaphragm at different positions inside GHT and without GHT.

diaphragm under an incident plane wave when the sensor was located at different positions of the glass horn. It can be seen that the amplitude of the deflection of the diaphragm decreases as the position z of the FP sensor inside the horn increases, but is significantly larger than that of the sensor without the glass horn. By optimizing the thickness, diameter of the diaphragm and the spacing of the adjacent pillars, the resonant frequency can be tuned to match the maximum pressure gain of the GHT.

Next, the parameters of the GHT are investigated. A constant $r_a = 0.4$ mm was used due to the fabrication issue. The pressure gain versus various H and r_g was simulated when the sensor was set at z = 0 mm. Fig. 4(a) shows the pressure gain at a frequency ranging from 10 kHz to 1 MHz when r_g is 2 mm and H is 3 mm, 4 mm and 5 mm, respectively. It shows that the pressure gain increases as the frequency increases, and this gain varies a lot when the frequency is below 500 kHz. Fig. 4(b) shows that the gain increases as r_g increases within a frequency range

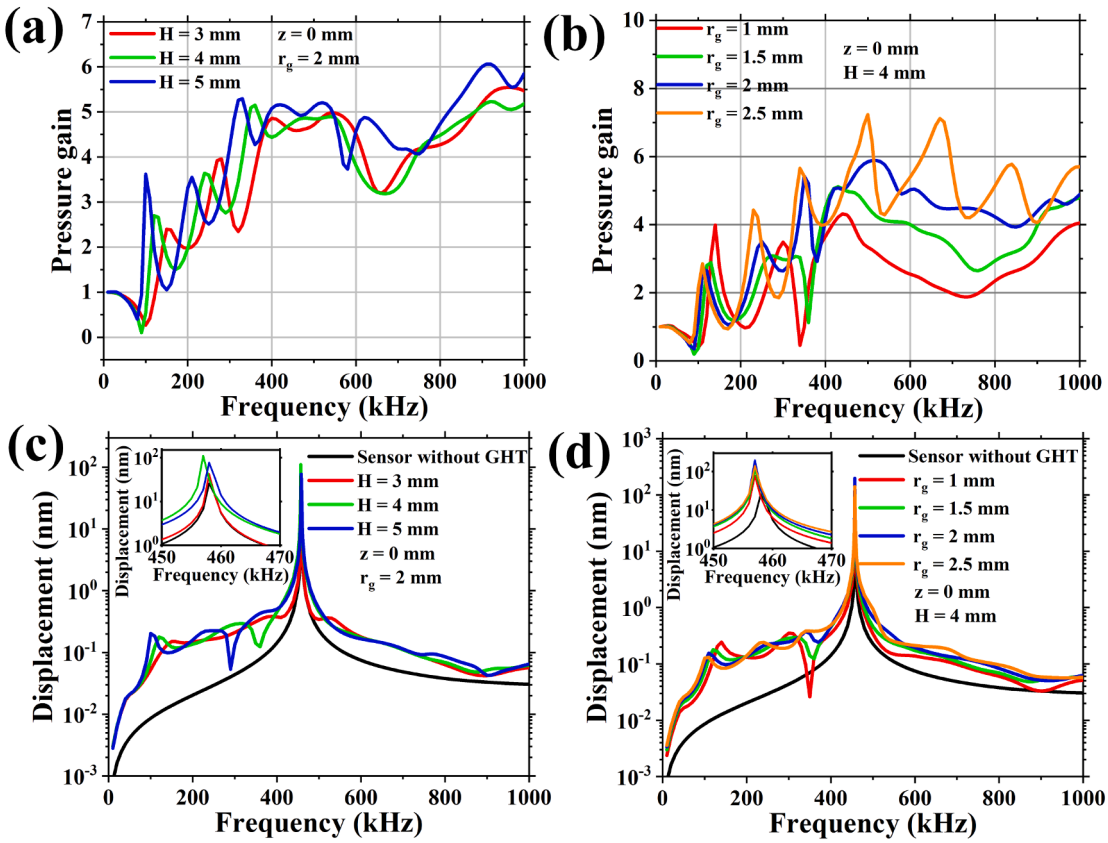

Fig. 4. Influences of the parameters of the GHT on the pressure gain and displacements of the sensor. (a) The pressure gain along the z-axis with different H from 10 kHz to 1 MHz when $r_g = 2$ mm. (b) The pressure gain along the z-axis with different r_g from 10 kHz to 1 MHz when H = 4 mm. (c) The comparison between simulated displacements of the bare sensor and assembled sensor with GHT of different H. (d) The comparison between simulated displacements of the bare sensor and assembled sensor with GHT of different r_g.

from 500 kHz to 1 MHz.

Combining these geometry parameters of GHT with the sensor, the displacements of the sensor with and without the glass tube is compared, as illustrated in Fig. 4(c) and (d). The position of sensor is chosen to be z = 0 mm for comparison. The results verify the displacements can be relatively improved inside the GHT at non-resonant frequencies. Also, the maximum displacement of 199 nm was achieved with $r_g = 2$ mm and H = 4 mm at the resonant frequency, which is magnified by a factor of 7.71 compared to the displacements of 25.8 nm without GHT. Based on the simulation, the structure of the glass tube can be optimized to enhance the pressure gain, when the frequency matches the resonant frequency of the FP sensor. In this work, r_g, r_a and H are 2 mm, 0.4 mm and 4 mm, respectively, in the following experiments.

3. Fabrication and experiments

3.1. FP sensor fabrication process

The proposed FP sensor is fabricated by a two-photon 3D printing system (photonic professional GT II, Nanoscribe GmbH), which includes

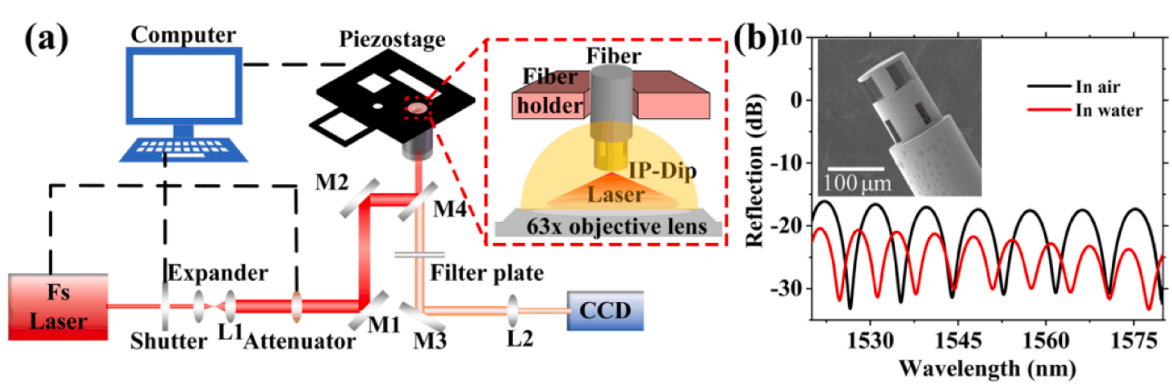

Fig. 5. The Schematic diaphragm of the 3D printing process on fiber tip. (a) Schematic diaphragm of printing ultrasonic sensor on the fiber tip based on the TPP lithography system, where L1 and L2 are lens, and M1, M2, M3 and M4 are reflective mirrors. (b) The SEM image and reflection spectra of the FP sensor in air and water.

3 process steps. (1) The cleaved single-mode fiber was placed on a customized fiber holder and immersed into a drop of photoresist, which was prepared on a 63 × objective lens. The femtosecond laser was focused on the fiber end facet through the objective lens by adjusting the alignment system. The designed sensor was fabricated by the focused laser beam in a layer-by-layer scanning manner (Fig. 5(a)). During the fabrication, the slicing and hatching distance of the device model were set as 100 nm. The writing speed and the femtosecond laser power were 5000 μm /s and 35 mW, respectively. It took about two hours for fabrication. (2) After fabrication, the sample was firstly developed by the propylene glycol methyl ether acetate (PGMEA) for 20 min and then rinsed by isopropyl alcohol (IPA) for 5 min. (3) Due to the fragility of the fabricated sensor on the fiber tip, the sensor may fall off from the fiber or even be destroyed by accidental impinging and violent shaking. A drop of ultraviolet (UV)-curable glue is applied on the connections between the fiber end facet and the printed device by a tapered fiber-based arm and then cured by a UV light for 10 min to improve the sensor's mechanical stability. Compared with the FP sensor in air, the fringe contrast in water decreases slightly, as shown in Fig. 5(b).The calculated cavity lengths are 140.09 μm and 135.43 μm in air and water based on fast Fourier transform (FFT) of the interference spectrum, which is very close to the designed FP cavity length of 140 μm. The inset of Fig. 5(b) shows a scanning electron microscopic (SEM) image of the printed sensor on the fiber tip. The diameter, thickness of the diaphragm and the distance between the pillars of the sensor are 100 μm, 5 μm and 50 μm, respectively.

3.2. Experiments and results

The schematic diagram of the experimental setup for testing the assembled sensor is shown in Fig. 6, which consists of a tunable laser (TSL, TUNICS T100S-HP), a fiber optic circulator, a photoelectric detector (Thorlabs, PDA05CF2 Amplified Detector), an oscilloscope (SIGLENT, SDS5034X), a piezoelectric transducer with a central frequency of 500 kHz (OLYMPUS, SU-318) and a function generator. The laser is tuned to a certain wavelength to make sure the phase is at the Q-point. The FP sensor and GHT are placed parallelly and aligned to the center of the transducer at the same level in water environment. The sensor was kept at a fixed position while the GHT attached to the holder of the motor can be moved. The transducer is driven by a function generator. During the testing process, the distance between the transducer and the FP sensor should be kept constant and the detected signals are recorded by the oscilloscope. The initial position of the FP sensor is located at z = 10 mm. The GHT is moved by driving the motor, the relative position z of the FP sensor inside the GHT is changed, which will help to find the precise position of the maximum pressure gain to enhance the sensor's pressure sensitivity.

To testify the frequency response of the proposed device, a burst signal of 100 kHz is applied to the sensor without the GHT. Fig. 7(a) shows the detected time signal and frequency spectrum of the sensor, which can achieve a signal-to-noise ratio (SNR) of 29.2 dB when acoustic pressure is 13.6 Pa. Hence, the noise-limited minimum detectable pressure level is measured as 4.71 mPa/Hz$^{1/2}$ @100 kHz with a resolution bandwidth of 10 kHz. Next, a periodic burst sinusoidal signal with a voltage of 10 Vpp is generated. When the GHT approaches to the FP sensor, the time domain detected burst signals are recorded. Fig. 7(b) shows the output voltage detected by the photoelectric detector, which shows the amplitude is sharply increased from the peak voltage of 1.7 mV to 6.81 mV when z is changed from 10 mm to 0 mm at a frequency of 500 kHz. The intensity of the detected signal is amplified by 4 folds than that of the sensor without the GHT in water.

The normalized signal gain versus the GHT position at different frequencies are shown in Fig. 7(c). When z is 4 mm, the FP sensor reaches the opening face of the GHT. It can be seen that the signal gain can achieve the maximum value when the sensor approaches at the bottom of the GHT. Noted that the normalized signal gain is smaller than 1 when the sensor is inside the GHT, which may be induced by the multi-reflection acoustic wave from the inner side wall of the GHT according to the simulated position of the scattered acoustic wave. Above all, we can take the position of the maximum normalized signal gain as the ideal position for the sound focusing, which can greatly enhance the weak wave pressure detection. After fixing the relative position between the FP sensor and the GHT, the assembled sensor can be directly tested in the water.

To test the frequency response of the designed FP sensor around its resonant frequency, the fixed sensor is placed at z = 0 mm. A pulser was connected to the transducer to generate a relative broadband acoustic wave. Fig. 8(a) and (b) show the time domain signal and corresponding FFT of the transducer and the FP sensor located at z = 0 mm, respectively. Compared with the transducer, the results indicate the probe sensor has a resonant peak at the frequency of 476.84 kHz with a −3 dB bandwidth of 366.05 kHz, which is comparable with the simulation. Noted that the probe sensor has a wider bandwidth than the transducer, indicating that the proposed sensor can be used for acoustic wave detection. Additionally, although the acoustic wave transmission loss is small due to the open-cavity structure of the probe device as the liquid can flow in the device, it causes some problems if the device is not fully filled with liquid. In future, a specific packaging with suitable structure and material can be designed for the proposed device.

4. Conclusion

In conclusion, a novel assembled FP acoustic sensor was designed and fabricated. The micro-resonant cavity supported by pillars was

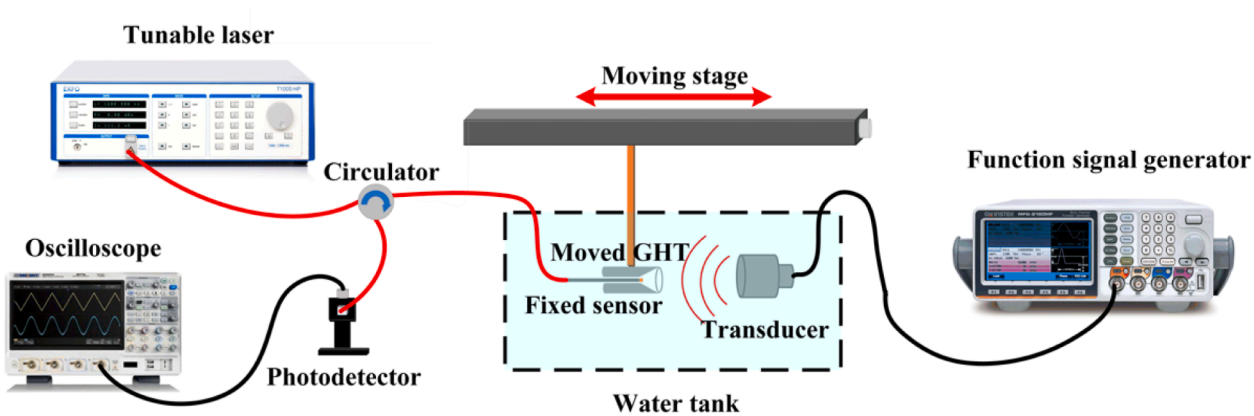

Fig. 6. The experimental setup for the frequency response of the assembled sensor.

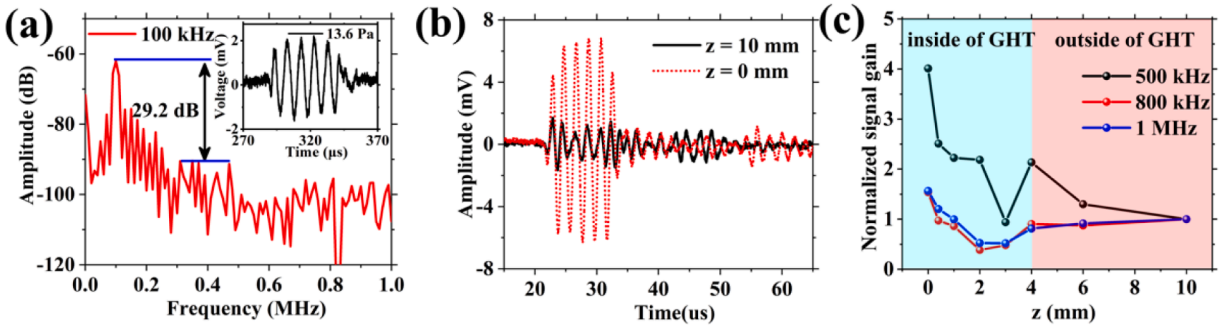

Fig. 7. The comparison between the response of the sensors with and without GHT. (a)The detected 100 kHz burst signal and frequency response. (b) The detected 500 kHz burst sinusoidal signals of the assembled sensor when z = 0 mm and z = 10 mm, respectively. (c)The output peak voltage of the assembled sensor with different frequencies at different position.

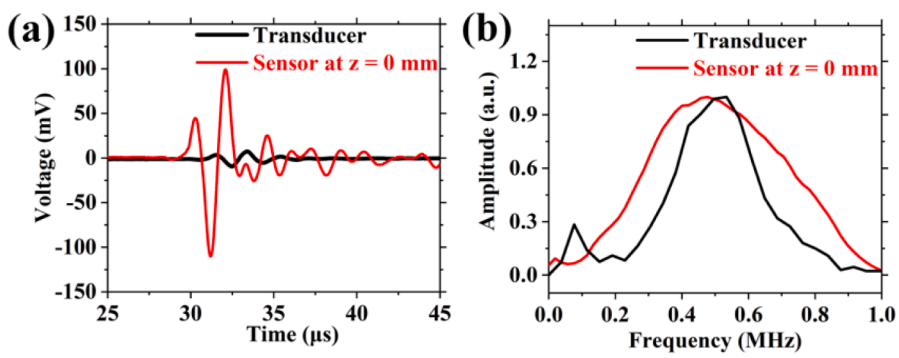

Fig. 8. The detected pulse response signals of the sensor and transducer. (a) The time-domain waveform of the pulse response signals of the transducer and the probe sensor when z = 0 mm, respectively. (b) The FFT of pulse response signals in (a).

manufactured by the two-photon direct laser writing, which is a simple and effective process to print micro-structure on the fiber tip. The results showed the sensor has a low noise-limited minimum detectable pressure level of 4.71 mPa/Hz$^{1/2}$@100 kHz, and the assembled FP sensor with an GHT has a resonant frequency of 476.84 kHz with a −3dB bandwidth of 366.05 kHz and a high pressure sensitivity, which is amplified by 4 times with respect to that of the FP sensor without GHT. The proposed sensor has great potential in the applications of imaging, structure health monitoring and non-destructive detection.

CRediT authorship contribution statement

Heming Wei: Investigation, Methodology, Formal analysis, Resources, Writing – review & editing, Supervision. **Zhangli Wu:** Writing – original draft, Methodology, Visualization. **Yan Wei:** Methodology, Validation. **Chen Wang:** Investigation, Validation. **Haiyan Zhang:** Methodology, Validation. **Fufei Pang:** Conceptualization, Validation. **Carlos Marques:** Investigation, Writing – review & editing. **Christophe Caucheteur:** Investigation, Writing – review & editing, Validation. **Xuehao Hu:** Investigation, Writing – review & editing, Validation.

Declaration of Competing Interest

The authors declare that they have no known competing financial interests or personal relationships that could have appeared to influence the work reported in this paper.

Data availability

Data will be made available on request.

Acknowledgments

H. Wei acknowledges the supports by the National Natural Science Foundation of China under Grant 62005153 and in part by the Natural Science Foundation of Shanghai, China, under Grant 20ZR1420300." Carlos Marques was supported by research actions 2021.00667.CEECIND (iAqua project), and projects i3N (LA/P/0037/2020, UIDB/50025/2020, and UIDP/50025/2020) and DigiAqua (PTDC/EEI-EEE/0415/2021), financed by national funds through the (Portuguese Science and Technology Foundation/MCTES (FCT I.P.). The Fonds de la Recherche Scientifique (F.R.S.-FNRS) under the Postdoctoral Researcher grant (Chargé de Recherches) of Xuehao Hu and the Senior Research Associate Position of Christophe Caucheteur.

References

[1] K.M. Holford, M.J. Eaton, J.J. Hensman, R. Pullin, S.L. Evans, N. Dervilis, K. Worden, A new methodology for automating acoustic emission detection of metallic fatigue fractures in highly demanding aerospace environments: An overview, Prog. Aerosp. Sci. 90 (2017) 1–11.
[2] I.M. De Rosa, C. Santulli, F. Sarasini, Acoustic emission for monitoring the mechanical behaviour of natural fibre composites: A literature review, Compos. A Appl. Sci. Manuf. 40 (9) (2009) 1456–1469.
[3] D.C. Whittingslow, H.K. Jeong, V.G. Ganti, N.J. Kirkpatrick, G.F. Kogler, O.T. Inan, Acoustic emissions as a non-invasive biomarker of the structural health of the knee, Ann. Biomed. Eng. 48 (1) (2020) 225–235.
[4] K. Ono, Review on structural health evaluation with acoustic emission, Appl. Sci. 8 (6) (2018) 958.
[5] B. Dong, C. Sun, H.F. Zhang, Optical detection of ultrasound in photoacoustic imaging, I.E.E.E. Trans. Biomed. Eng. 64 (1) (2017) 4–15.
[6] S. Preisser, W. Rohringer, M. Liu, C. Kollmann, S. Zotter, B. Fischer, W. Drexler, All-optical highly sensitive akinetic sensor for ultrasound detection and photoacoustic imaging, Biomed. Opt. Express 7 (10) (2016) 4171–4186.
[7] T. Zhao, L. Su, W. Xia, Optical ultrasound generation and detection for intravascular imaging: A review, J. Healthc. Eng. 2018 (2018) 1–14.

[8] J.M. Lopez-Higuera, L. Rodriguez Cobo, A. Quintela Incera, A. Cobo, Fiber optic sensors in structural health monitoring, J. Light. Technol. 29 (4) (2011) 587–608.
[9] H. Li, X. Wang, D. Li, J. Lv, Y. Yu, Mems-on-fiber sensor combining silicon diaphragm and supporting beams for on-line partial discharges monitoring, Opt. Express 28 (20) (2020) 29368–29376.
[10] H. Saheban, Z. Kordrostami, Hydrophones, fundamental features, design considerations, and various structures: A review, Sens. Actuator A: Phys. 329 (2021), 112790.
[11] A. Pohl, R. Oliveira, R. Silva, C. Marques, P. Neves, K. Cook, J. Canning, R. Nogueira, Advances and new applications using the acousto-optic effect in optical fibers, Photonic Sensors 3 (1) (2013) 1.
[12] C. Marques, L. Bilro, L. Kahn, R. Oliveira, D. Webb, R. Nogueira, Acousto-Optic Effect in Microstructured Polymer Fiber Bragg Gratings: Simulation and Experimental Overview, Journal of Lightwave Technology 31 (10) (2013) 1551.
[13] H. Wei, S. Krishnaswamy, Adaptive fiber-ring lasers based on an optical fiber Fabry-Perot cavity for high-frequency dynamic strain sensing, Appl. Opt. 59 (2) (2020) 530–535.
[14] P.A. Fomitchov, S. Krishnaswamy, J.D. Achenbach, Compact phase-shifted Sagnac interferometer for ultrasound detection, Opt. Laser Technol. 29 (6) (1997) 333–338.
[15] P. Fan, W. Yan, P. Lu, W. Zhang, W. Zhang, X. Fu, J. Zhang, High sensitivity fiber-optic Michelson interferometric low-frequency acoustic sensor based on a gold diaphragm, Opt. Express 28 (17) (2020) 25238–25249.
[16] C. Zhang, S.L. Chen, T. Ling, L.J. Guo, Review of imprinted polymer microrings as ultrasound detectors: Design, fabrication, and characterization, IEEE Sens. J. 15 (6) (2015) 3241–3248.
[17] H. Wei, S. Krishnaswamy, Polymer micro-ring resonator integrated with a fiber ring laser for ultrasound detection, Opt. Lett. 42 (13) (2017) 2655–2658.
[18] W.J. Westerveld, M. Mahmud-Ul-Hasan, R. Shnaiderman, V. Ntziachristos, X. Rottenberg, S. Severi, V. Rochus, Sensitive, small, broadband and scalable optomechanical ultrasound sensor in silicon photonics, Nat. Photonics 15 (5) (2021) 341–345.
[19] H. Wei, C. Tao, Y. Zhu, S. Krishnaswamy, Fiber Bragg grating dynamic strain sensor using an adaptive reflective semiconductor optical amplifier source, Appl. Opt. 55 (10) (2016) 2752–2759.
[20] H. Wei, Z. Gong, W. Wu, J. Che, L. Zhang, F. Pang, T. Wang, Broadband fiber-optic acoustic sensors, J. Light. Technol. 40 (12) (2022) 4033–4041.
[21] H. Yin, Z. Shao, F. Chen, X. Qiao, Highly sensitive ultrasonic sensor based on polymer Bragg grating and its application for 3D imaging of seismic physical model, J. Light. Technol. 40 (15) (2022) 5294–5299.
[22] H. Wei, S. Krishnaswamy, Direct laser writing of a phase-shifted Bragg grating waveguide for ultrasound detection, Opt. Lett. 44 (15) (2019) 3817–3820.
[23] L. Macedo, E. Pedruzzi, L. Avellar, C. Castellani, M. Segatto, A. Frizera, C. Marques, A. Leal-Junior, High-resolution sensors for mass deposition and low-frequency vibration based on phase-shifted Bragg gratings, IEEE Sens. J. 22 (3) (2023) 2228–2235.
[24] W. Zhang, P. Lu, W. Ni, W. Xiong, D. Liu, J. Zhang, Gold-diaphragm based Fabry-Perot ultrasonic sensor for partial discharge detection and localization, IEEE Photon. J. 12 (3) (2020) 1–12.
[25] J. Liu, L. Yuan, J. Lei, W. Zhu, B. Cheng, Q. Zhang, Y. Song, C. Chen, H. Xiao, Micro-cantilever-based fiber optic hydrophone fabricated by a femtosecond laser, Opt. Lett. 42 (13) (2017) 2459–2462.
[26] Y. Wu, C. Yu, F. Wu, C. Li, J. Zhou, Y. Gong, Y. Rao, Y. Chen, A highly sensitive fiber-optic microphone based on graphene oxide membrane, J. Light. Technol. 35 (19) (2017) 4344–4349.
[27] W. Ni, P. Lu, X. Fu, W. Zhang, P.P. Shum, H. Sun, C. Yang, D. Liu, J. Zhang, Ultrathin graphene diaphragm-based extrinsic Fabry-Perot interferometer for ultra-wideband fiber optic acoustic sensing, Opt. Express 26 (16) (2018) 20758–20767.
[28] Y. Miida, Y. Matsuura, All-optical photoacoustic imaging system using fiber ultrasound probe and hollow optical fiber bundle, Opt. Express 21 (19) (2013) 22023–22033.
[29] Y. Sun, Z. Dong, Z. Ding, N. Wang, L. Sun, H. Wei, G.P. Wang, Carbon nanocoils and polyvinyl alcohol composite films for fiber-optic Fabry-Perot acoustic sensors, Coatings 12 (10) (2022) 1599.
[30] C. Li, S. Lu, C. Zhong, X. Song, High-sensitivity low-frequency Fabry-Perot ultrasonic hydrophone with chitosan diaphragm, IEEE Sens. J. 22 (7) (2022) 6669–6676.
[31] S. Wang, W. Chen, A large-area and nanoscale graphene oxide diaphragm-based extrinsic fiber-optic Fabry-Perot acoustic sensor applied for partial discharge detection in air, Nanomaterials (Basel) 10 (11) (2020) 2312.
[32] M. Yao, Y. Zhang, X. Ouyang, A. Ping Zhang, H.-Y. Tam, P.K.A. Wai, Ultracompact optical fiber acoustic sensors based on a fiber-top spirally-suspended optomechanical microresonator, Opt. Lett. 45 (13) (2020) 3516–3519.
[33] W. Yang, C. Zhang, J. Zeng, W. Song, Ultrasonic signal detection based on Fabry-Perot cavity sensor, Vis. Comput. Ind. Biomed. Art 4 (1) (2021) 4–9.
[34] J.A. Guggenheim, J. Li, T.J. Allen, R.J. Colchester, S. Noimark, O. Ogunlade, I. P. Parkin, I. Papakonstantinou, A.E. Desjardins, E.Z. Zhang, P.C. Beard, Ultrasensitive plano-concave optical microresonators for ultrasound sensing, Nat. Photonics 11 (11) (2017) 714–719.
[35] C. Xiong, C.R. Liao, Z.Y. Li, K.M. Yang, M. Zhu, Y.Y. Zhao, Y.P. Wang, Optical Fiber Integrated Functional Micro-/Nanostructure Induced by Two-Photon Polymerization, Front. Mater. 7 (2020), 586496.
[36] H. Wei, M. Chen, S. Krishnaswamy, Three-Dimensional-Printed Fabry-Perot Interferometer on an Optical Fiber Tip for a Gas Pressure Sensor, Appl. Opt. 59 (7) (2020) 2173–2178.
[37] Q. Rong, R. Zhou, Y. Hao, X. Yin, Z. Shao, T. Gang, X. Qiao, Ultrasonic sensitivity-improved Fabry-Perot interferometer using acoustic focusing and its application for noncontact imaging, IEEE Photon. J. 9 (3) (2017) 1–11.
[38] H. Li, J. Bu, W. Li, J. Lv, X. Wang, K. Hu, Y. Yu, Fiber optic Fabry-Perot sensor that can amplify ultrasonic wave for an enhanced partial discharge detection, Sci. Rep. 11 (1) (2021) 8661.
[39] Y. Chen, H. Liu, M. Reilly, H. Bae, M. Yu, Enhanced acoustic sensing through wave compression and pressure amplification in anisotropic metamaterials, Nat. Commun. 5 (2014) 5247.
[40] G. Yin, P. Li, X. Yang, and J. Guo, "Design and investigation of funnel for acoustic wave," in 2021 IEEE International Ultrasonics Symposium (IUS) (2021), pp. 1-4.
[41] E.D. Lemma, F. Rizzi, T. Dattoma, B. Spagnolo, L. Sileo, A. Qualtieri, M. De Vittorio, F. Pisanello, Mechanical properties tunability of three-dimensional polymeric structures in two-photon lithography, IEEE Trans. Nanotechnol. 16 (1) (2016) 23–31.